

Tracking of Hematopoietic Stem Cells in Microscopy Images for Lineage Determination

Sungeun Eom, Seung-il Huh, Dai Fei Elmer Ker, Ryoma Bise, Takeo Kanade

Abstract—Hematopoietic stem cells (HSCs) are blood-forming stem cells that give rise to all blood cell types and are routinely used in therapies today. However, HSCs have a limited capability to expand *ex vivo*. This paper presents an automated tracking method that will facilitate the study and expansion of HSCs by monitoring the behavior of the cells *in vitro* under serum-free media conditions using phase contrast microscopy. The proposed method exploits a data-association approach that consists of detection and tracking modules. Given an input image sequence, cell positions are first located in each frame by using ring filters of multiple sizes. The detected cells are then associated across consecutive frames for tracking. Each of the newly appeared cells found during the association is examined whether it is a newborn cell as a result of mitosis by using an event detection conditional random field (EDCRF). Our tracking method is evaluated with four sequences of 11520 frames in terms of track purity and target effectiveness, achieving 88.3% and 92.8%, respectively.

Index Terms—Cell tracking, ring filter, data association, mitosis detection, hematopoietic stem cells.

I. INTRODUCTION

HEMATOPOIETIC stem cells (HSCs) are a heterogeneous population of multipotent stem cells that give rise to all blood cell types in the body. They can be isolated from a variety of sources including bone marrow, umbilical cord blood and fetal liver [1], [2], [3], [4]. Transplantation of HSCs has been ongoing for the last 30 years, and is presently used in a wide range of medical conditions, including bone marrow failure as well as rescuing hematopoietic function for blood disorders [5], [6].

One of the major limitations to HSC therapy is the low cell dose available for transplantation, particularly where HSCs are isolated from umbilical cord blood [7], [3]. As a result, a great deal of research effort has focused on optimizing the *in vitro* expansion of HSCs while maintaining their stem cell characteristics such as the capability to differentiate into different blood cell types. To achieve this goal, it is important to study and identify the various culture conditions that would alter HSC population kinetics to produce large numbers of clinical grade HSCs [6].

We present an automated tracking method that is capable of real-time monitoring of HSC behaviors. The ability to track individual stem cells *in vitro* over time and subsequently construct cell lineage trees would promote a deeper understanding of stem cell behavior both at the single cell level as well as the population level. This is especially critical in the application of HSC expansion since current culture techniques are not able to maintain the HSCs' ability to repopulate the body over the long term.

Many tracking methods have been proposed for analyzing the behavior of cell populations. They can be roughly classified into two groups: contour-evolution approach and data-association approach.

The contour-evolution approach is widely used in cell segmentation and tracking [8], [9], [10], [11], [12]. In this approach, tracking is performed by finding cell boundaries in the current frame typically by such techniques as active contour or level set, starting with cell boundaries in the previous frame. This approach can nicely handle geometrical and topological changes of cell shape, but it often fails to detect and track new cells that are born through mitosis. To connect the newborn cells to its mother cell, one can use a linking algorithm [8] or event detection methods [9], [10], [11] that explicitly recognize the mitotic cells based on their features, such as intensity, area, circularity, and local variance. Coupled active surfaces are also used for detecting dividing cells in 3-D microscopy [12].

Another approach is the data-association approach [13], [14], [15], [16], [17], [18]. This approach first detects and/or segments cells frame by frame, and then associates them by using their relationships over two or more consecutive frames. This association is often formulated as a one-to-one assignment problem [13]. One-to-two assignment [14] is also considered in order to handle dividing cells. Alternatively, the association is solved with the maximum *a posteriori* estimation [15]. Overlapping cells are the source of difficulty in the data association approach because both many-to-one and one-to-many assignments should be taken into consideration. One method to deal with them is a multi-assignment algorithm [16] which consists of a sequence of one-to-one assignments and a modified PDA filter. A graph-theoretic tracking method [17] tackles overlapping as well as dividing cells by extending the minimum-cost flow algorithm [19]. To track the overlapping cells more reliably, partial contour matching based on contour shapes is presented [18]. It enables to keep tracking a cluster formed by multiple cells that are touching or partially overlapping to each other.

In this paper, we propose a tracking-by-detection method suitable for HSC populations. The contributions of the method are as follows:

1) *Detection*: Under a phase contrast microscope, HSCs typically appear as round objects of various sizes surrounded by bright halos (Fig. 1). There are two standard methods that can be applied to detect such objects: Hough transform and correlation. Hough transform based detection methods [20], [21], [22], which use image gradient or edge information, have some drawbacks in our case due to the variations of

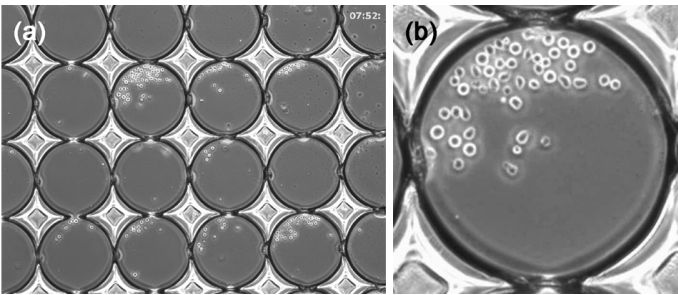


Fig. 1. HSCs imaged with phase contrast microscopy. (a) HSC populations in a microwell array. (b) HSC population confined in a single microwell.

cell shape and appearance. The variations cause low peaks in an output accumulator space and thus lead to false negatives or inaccurate detection. Correlation based methods [23], [24], [25], [26] partly overcome those drawbacks by using cell image templates, but still show some limitations. First, false positives tend to occur around the cells when cells are closely located and their halos happen to form a partial cell pattern. As the number of cells increases, such false positives will appear more often. Second, a cell can be detected multiple times by templates with slightly different sizes, which also produce high responses. To address the drawbacks of the correlation methods, we propose a detection method using a ring filter bank with a peak detection rule, which considers the output pattern of the filter responses and the curvature of cell boundaries [27].

2) *Tracking*: We adopt a data-association approach to connect observations obtained from the detection. The simplest association is to connect observations using a single frame [13], [14]. In other words, all possible events are determined between two consecutive frames. Once it fails to track a cell in a certain frame, it would be hard to recover the lost track in the next frames. The most sophisticated association is to consider all possible combinations over multiple consecutive frames and choose the best one [28], which is combinatorially expensive. In our case, we found that migrating cells can be tracked well using a single frame thanks to the detection results in high accuracy, but mitosis (cell birth) and apoptosis (cell death) are not easy to determine with a single-frame association. Therefore, migrating cells are found by one-to-one correspondence through a frame-by-frame association, while none-to-one (extra cells) and one-to-none (extra tracks) cases are examined over multiple frames to confirm mitosis and apoptosis. In particular, mitosis is examined spatio-temporally. A patch sequence that potentially contains a mitosis event is first extracted, and the sequence is evaluated by an event-detection conditional-random field (EDCRF) [29]. With this procedure, correct linking between mother and daughter cells is achieved. The total tracking results are represented by lineage trees that record a complete history of cell growth: how they move (location and size of each cell in each image) and how they proliferate (location and timing of mitosis resultant and mother-daughter relationships).

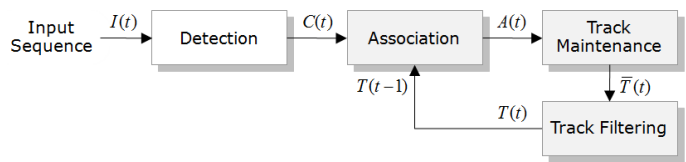


Fig. 2. Overview of our tracking method.

II. METHODS

Fig. 2 shows an overview of our tracking method. Given an input image sequence, cell positions are first located in each frame by using ring filters of multiple sizes. Once cells are detected, they are connected across consecutive frames by one-to-one assignment in the association. Extra cells and extra tracks that are not assigned to any track or any cell are dealt with in the following track maintenance. The last positions of tracks are filtered for the next association in the subsequent frame. The details of each step are described in the following subsections.

A. Detection

1) *Multiple-Radius Ring Filtering*: As depicted in Fig. 3(a), the shape and appearance of HSCs can be modeled by a ring pattern which is a bright ring on a dark background. Let us denote the outer radius of the ring by r_c and the width of the ring by w , then the model has the following form:

$$Cell(x, y; r_c, w) = circ(x, y; r_c) - circ(x, y; r_c - w), \quad (1)$$

where

$$circ(x, y; r) = \begin{cases} 1 & \text{if } \sqrt{x^2 + y^2} \leq r \\ 0 & \text{otherwise.} \end{cases} \quad (2)$$

Cell radius, r_c , changes between 9 and 15 pixels ($5.5\mu\text{m}$ and $9.2\mu\text{m}$) and the width of halo, w , is approximately constant and set to be 6 pixels ($3.7\mu\text{m}$) in our experiments.

In order to detect the pattern, we design multiple-radius ring filters that have identical profile as the pattern; the optimal filter for detecting a pattern is the pattern itself [30]. The filter

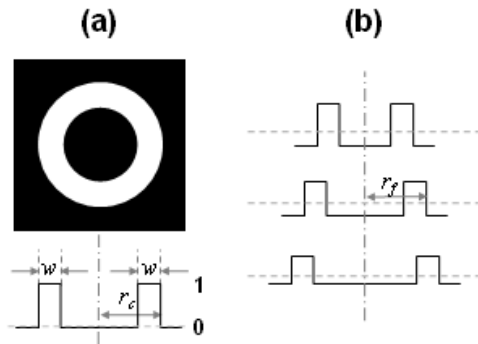


Fig. 3. (a) Input ring pattern as a cell model. (b) Cross-sections of the ring filters with different radii that have identical profile as the input pattern but are normalized to give the same magnitude responses for each matched ring size.

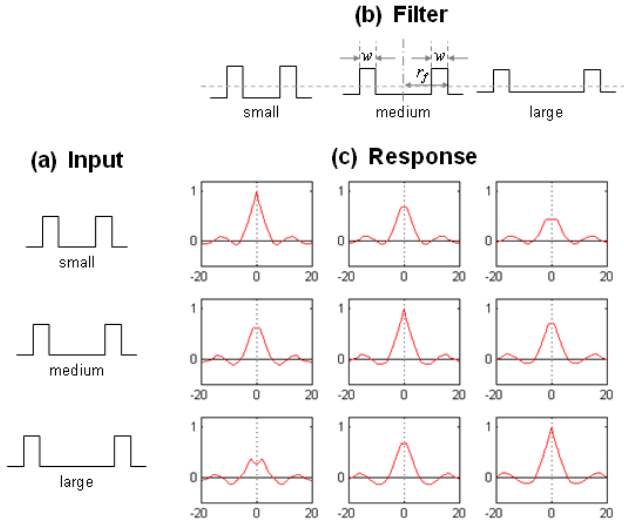


Fig. 4. Output variations of a multiple-radius ring filter bank. (a) Input ring patterns with different radii. (b) A multiple-radius ring filter bank. (c) The outputs of the filter bank applied to each ring pattern. The same maximum peak of 1 occurs when the filter exactly matches the input, and lower peaks are generated when the filter slightly mismatches the input.

is represented as follows:

$$\text{RingFilter}(x, y; r_f, w) = \frac{\text{Cell}(x, y; r_f, w) - M}{S(1 - M)}, \quad (3)$$

$$-D/2 \leq x, y \leq D/2,$$

where D is the width of the filter, S is the ring area, and M is the mean of the square filter, S/D^2 . The filter size D is set to be $2(r_f + 2)$. The filter has a zero mean and are normalized to give the same magnitude responses for each matched cell size. If an input ring pattern is correlated with the exactly same unnormalized one as a filter, the response will increase as the ring size increases. This is undesirable because we need to measure how well they match each other regardless of the ring size. Fig. 3(b) shows the cross-sections of the normalized ring filters with different radii.

When the normalized filter with radius r_f is applied to an ring pattern with radius r_c , the output is

$$\begin{aligned} I_f(x, y; r_f, r_c) &= \text{RingFilter}(x, y; r_f, w) \star \text{Cell}(x, y; r_c, w) \\ &= \sum_{i, j=-D/2}^{D/2} \frac{\text{Cell}(i, j; r_f, w) - M}{S(1 - M)} \cdot \text{Cell}(x + i, y + j; r_c, w) \\ &= S^+(x, y) \frac{1 - M}{S(1 - M)} - S^-(x, y) \frac{M}{S(1 - M)}, \end{aligned} \quad (4)$$

where S^+ is the input ring area overlapping the filter ring area and S^- is the rest of the input ring area under the filter. If the filter is exactly matched to the ring pattern, the output will reach the maximum 1 with $S^+ = S$ and $S^- = 0$. Fig. 4(c) shows the responses of the ring filters applied to ring patterns with different radii.

2) *Peak Detection*: As can be seen in the filter responses in Fig. 4, the highest peak occurs when the radius of the filter exactly matches that of the pattern, and lower peaks are generated when the filter slightly mismatches the pattern.

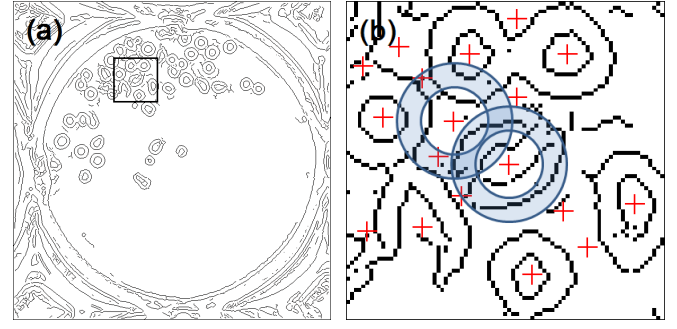


Fig. 5. (a) Edge image. (b) Edge segments in band area around a circle with radius r_c of the applied filter. If the peak, denoted with a red cross, corresponds to a true cell, the edge segments have positive curvature (convex) as in the lower band.

Therefore, the pattern can be located by detecting a peak in the radius space in addition to the 2D spatial space.

There is one characteristic of ring filters in that they can give high response at the locations surrounded by neighboring cells because they also form a similar pattern to the cell model as shown in Fig. 5(a). To address this problem, we examine cell boundaries by extracting edges from the input image. When the peaks are detected in the 2D spatial and radius spaces, we first draw a circle with radius r_c at the peak location and then find edge segments in the band area around the circle. The band areas for two peak locations are shown in Fig. 5(b); the width of the band is set to be 6 pixels ($3.7\mu\text{m}$) to accommodate the variations of cell shape and appearance. If the peak corresponds to a true cell, the edge segments on the band are expected to have positive curvature. Therefore, to eliminate the false positive, we use the length of the edge segments e_i with positive curvature:

$$R = \frac{\sum_{i=1}^N \text{Length}(e_i^{\text{pos}})}{2\pi r_c}, \quad (5)$$

Algorithm 1 Cell Detection

Input: image I ; cell radii $[r_1, \dots, r_n]$; thresholds th_1, th_2
Output: cell locations and radii $(\mathbf{p}_{\text{final}}, \mathbf{r}_{\text{final}})$

- 1) **Multiple-Radius Ring Filtering**
- 1: **for** $r \leftarrow r_1 - 1, \dots, r_n + 1$ **do** \triangleright ring filter's outer radii
- 2: $I_r \leftarrow \text{RINGFILTERING}(I, r)$
- 3: **end for**
- 2) **Peak Detection**
- 4: $I_{\text{edge}} \leftarrow \text{EDGEDETECTION}(I)$ \triangleright Fig. 5(a)
- 5: **for** $r \leftarrow r_1, \dots, r_n$ **do**
- 6: % find peaks in 2D spatial space as candidates
- 7: $p \leftarrow \text{PEAKDETECTION2DSPATIAL}(I_r, th_1)$
- 8: % fit a quadratic model to filter outputs at $p = (x, y)$
- 9: $P_{\{r-1, r, r+1\}} \leftarrow \text{QUADRATICFITTING}(I_{\{r-1, r, r+1\}}, p)$
- 10: % compute roundness in Eq. 5
- 11: $R \leftarrow R(I_{\text{edge}}, p, r)$
- 12: % validate candidates with a peak detection rule
- 13: $\{p_{\text{valid}}\}_r \leftarrow \text{PEAKDETECTIONRULE}(P, R, th_2)$
- 14: **end for**
- 15: $(\mathbf{p}_{\text{final}}, \mathbf{r}_{\text{final}}) \leftarrow \{p_{\text{valid}}\}_r$ for all r

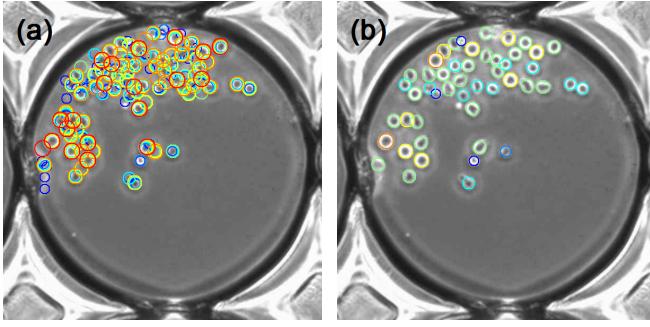


Fig. 6. (a) Cell candidates from ring filters with radii between 9 and 15 pixels ($5.5\mu\text{m}$ and $9.2\mu\text{m}$); different colors indicate different sizes. (b) Detection result after applying the peak detection rule to the candidates.

where $2\pi r_c$ is a normalization factor for each cell size.

In summary, given the ring filter outputs, to detect a cell with radius r_c , we find peaks, P_{r_c} in the 2D spatial output of the filter with radius r_c , satisfying the following peak detection rule:

$$P_{r_c} > P_{r_c \pm 1} \text{ and } P_{r_c} \times R > th. \quad (6)$$

To check the rule with peak curvatures, values, and locations in a higher resolution, a quadratic surface model can be fit to the filter outputs in a *fitting window* of $M \times M$ pixels around each peak location [27]. In other words, peak curvatures at a given location on the outputs of filters with radii $r_c - 1$, r_c , and $r_c + 1$ should be all negative (local maxima) and a peak value at radius r_c should be higher than peak values at radii $r_c \pm 1$. Peak locations are allowed to be slightly shifted within a certain distance from the original location.

More details on the detection procedure are described in Algorithm 1, where to reduce computational burden, cell candidate locations, p , are first obtained by detecting the peaks with values exceeding a preset threshold, th_1 , in each ring filter output; the threshold is set to be low enough to achieve a near-zero false negative rate, which ensures (almost) all cells are detected. True cells, p_{valid} , are then detected by imposing the peak detection rule. Fig. 6 shows the cell candidates and the detection result. It is shown that cells are successfully detected.

B. Association: Cell-Track Correspondence

The result of the detection is a set of cell locations and radii. The detected cells in each frame are associated with tracks that are established up to the previous frame. To associate the detected cells to the tracks, our tracking method uses a global nearest neighbor (GNN) approach.

Let us assume that N tracks ($T_i; i = 1, \dots, N$) have been established and M cells ($C_j; j = 1, \dots, M$) have been detected in the current frame. As illustrated in Fig. 7, we build an association matrix whose columns and rows represent cells, C_j and tracks, T_i , respectively. The (i, j) element of the matrix, P_{ij} , is the likelihood that track i is associated with cell j . The likelihood is based on the Euclidean distance d_{ij} between a cell and a track; other features, such as the morphological and brightness changes of HSCs, are not distinctive as shown in

	C_1	\dots	C_j	\dots	C_M	
T_1	P_{11}					
\vdots						
T_i				P_{ij}		
\vdots						
T_N				P_{NM}		

Fig. 7. Association matrix. Each column, C , corresponds to each cell detected in the current frame, each row, T , represents each track established up to the previous frame, and the element, P_{ij} , represents the likelihood of assigning cell j to track i . Given the matrix, the best combination between tracks and cells is found in terms of the likelihood.

Fig. 1. We choose the following likelihood:

$$P_{ij} = \begin{cases} e^{-a \cdot N_i} \cdot (1 - d_{ij}^2/G_i^2) & \text{if } d_{ij} \leq G_i \\ 0 & \text{otherwise} \end{cases} \quad (7)$$

where G_i is the maximum Euclidean distance that a track i can move between two consecutive frames, and N_i is the number of frames for which a track i is continuously unassociated with cells up to the previous frame. If the distance d_{ij} is greater than G_i , P_{ij} is set to be zero and the correspondence is ignored. The factor $e^{-a \cdot N_i}$ is multiplied to penalize tracks that failed to be associated for a certain period of time, where a is a constant [31]. For example, when two tracks are located at the same distance from a cell, if the first track is being associated and the second one is not being associated for the last frames, the first track has the priority over the second one to be associated with the cell.

Given the matrix with the likelihood, we consider two types of tracks to find cell-track correspondence: *confirmed* tracks and *tentative* tracks. When an extra observation appears, it is regarded as a tentative track and if the track is consistently associated (tracked) for 8 out of 10 frames, it becomes a confirmed track. If there are only confirmed tracks during asso-

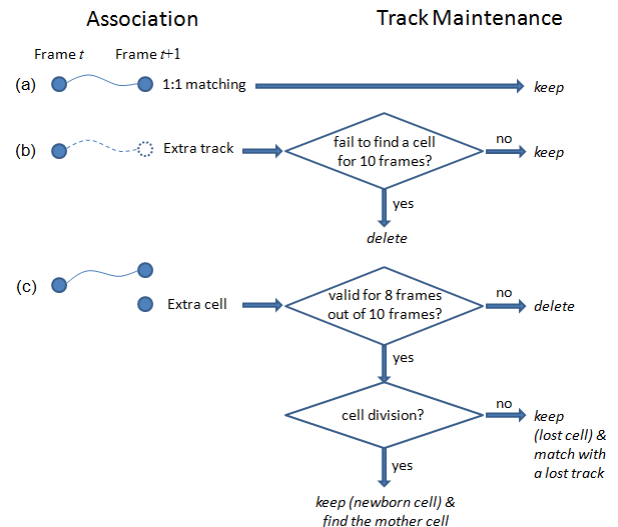


Fig. 8. Schematic diagram of track maintenance process for (a) 1:1 matching, (b) extra track, and (c) extra cell.

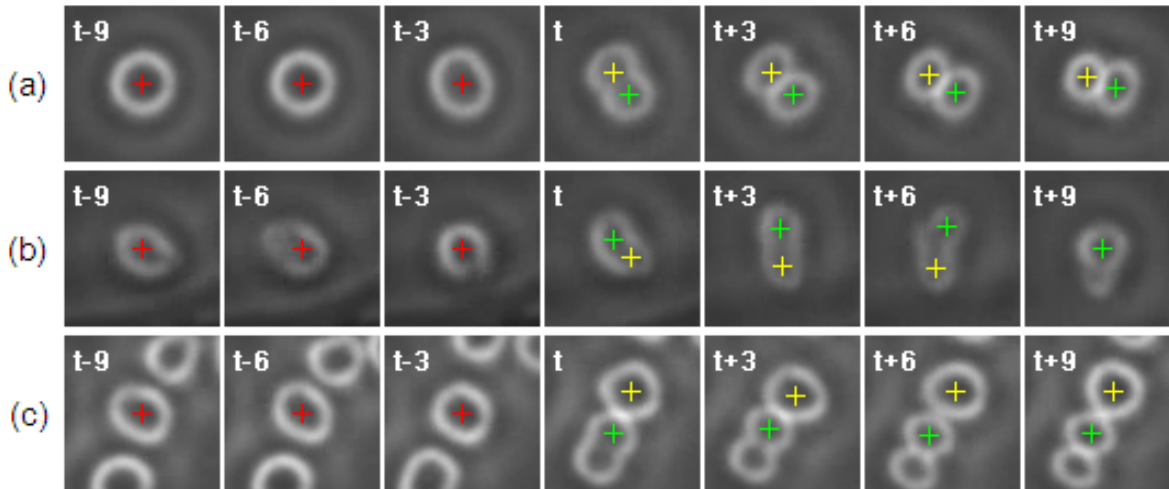


Fig. 9. Examples of patch sequences for mitosis detection. Green crosses indicate the centers of an extra cell, while red and yellow ones indicate those of possible mother and sibling cells of the extra cell, respectively. Along the tracks of the possible mother and daughter cells, patch sequences are extracted: (a) typical mitosis process, (b) an example that one cell is detected at two regions, and (c) an example that mother and sibling cells of the extra cell are incorrectly suggested due to the neighboring cell. Our mitosis detection helps to correctly determine the occurrence of mitosis as well as the identification of mother and daughter cells in such cases.

ciation, the correspondence between tracks and cells is found by maximizing the sum of likelihoods [32]. However, if there exist tentative tracks, confirmed tracks are first associated and then tentative tracks are separately associated during 10 frames to check whether they are cells or false positives. This two-step association prevents confirmed tracks from associating with false positives.

C. Track Maintenance

After association, track maintenance is followed to deal with extra tracks not assigned to a cell or extra cells not assigned to a track. Fig. 8 overviews the process of track maintenance. Each of the unassigned tracks is monitored for ten subsequent frames to find a cell to which the track can be assigned. If such a cell is not found, the track is considered false positive and deleted. For unassigned extra cells, a tentative track initiates from each of them and is monitored for ten subsequent frames. If a tentative track fails to be assigned to a cell for at least eight out of the ten frames, the tentative track and the corresponding extra cell are considered false positive and deleted. Otherwise, we keep the track and the extra cell, and subsequently examine whether the cell is a newborn cell as a result of mitosis. If it is determined to be a newborn cell, the mother-daughter relation is searched as well for lineage construction. Otherwise, the newly detected cell is regarded as a previously lost cell and its track is searched among the lost tracks.

1) *Mitosis Detection*: To determine whether an extra cell is a newborn cell or not, we construct patch sequences from the time and location that the extra cell is detected. Specifically, when an extra cell is first detected at frame t , we detect its candidate sibling cell that is in contact with the extra cell at the same frame. From the trajectory of the candidate sibling cell, at most 20 square patches from frame $t - 10$ through $t + 9$ are extracted as a mitosis candidate patch sequence. Fig. 9(a) shows a typical example of candidate patch sequence

when mitosis occurs. If either the extra cell or its sibling cell is not detected in certain frames among the 20 frames, patches from the frames are not used to construct the patch sequence. After patch sequence construction, unique scale gradient histograms [29] are extracted as visual features for each patch in patch sequences. After candidate patch sequence construction, mitosis detection reduces to a binary classification task whether each patch sequence contains a mitotic event or not. For this decision, Event Detection Conditional Random Field (EDCRF) [29] is adopted. To obtain training samples, from 10 HSC sequences, which were not used for our evaluation, candidate patch sequences were extracted and manually annotated.

This mitosis detection enables track maintenance to be more reliable. For example, when a cell elongates as shown in Fig. 9(b), the cell is often detected at two circular regions that may be regarded as two daughter cells even though no mitosis occurs. Mitosis detection enables to correctly recognize this false positive so as to avoid false trajectory branching. In addition, mitosis detection helps to identify correct mother and sibling cells when mitosis occurs close to another cell; when a new-born cell is in contact with another cell other than the true sibling cell as shown in Fig. 9(c), the identities of mother and sibling cells are often ambiguous. Mitosis detection resolves this confusion and aids to find correct mother and sibling cells.

D. Track Filtering

The filtering step estimates the states of assigned tracks in the track maintenance. The track estimates are important because the next association in a subsequent frame is affected by them. Fig. 10(a) shows the example. If the numbers, track IDs, are ignored, the green circles are exactly the same results from the detection. In tracking, a green color means to be continuously tracked and a red one in frame 590 to be missed at the moment. In frame 589 and 590, a cell corresponding

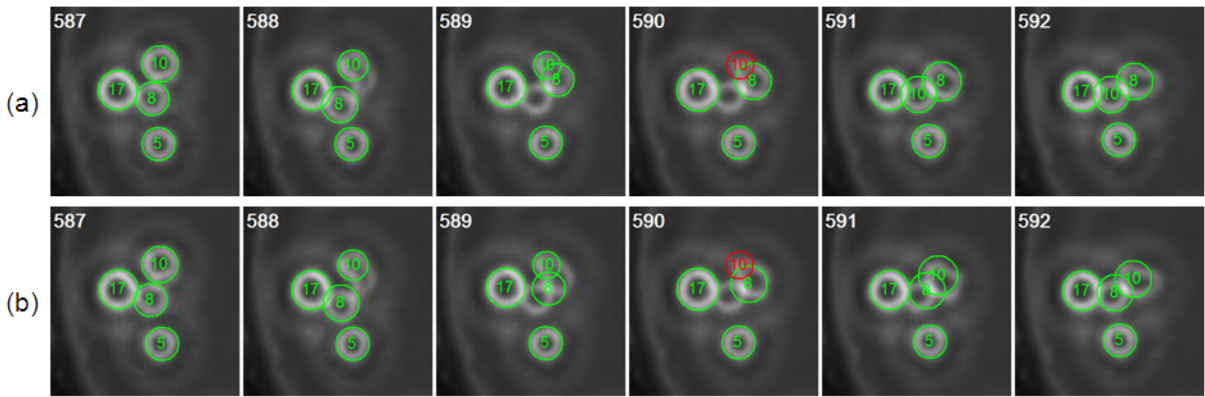


Fig. 10. Tracking (a) without and (b) with applying the Kalman filter; the numbers in circles represent track IDs and the red ones are temporarily lost tracks. The positions in (a) are exactly the same as the detection result, while the positions in (b) are corrected ones by the Kalman filter during tracking. When the filter is not applied, track 8 is switched with track 10 due to a false positive in the vicinity of a false negative in frame 589. On the other hand, the track switching is avoided with the filter that corrects the positions of track 8 in frame 589 and 590.

to track 8 in frame 588 is not detected and unfortunately a false positive appears around there in frame 589. In this case, if filtering is not applied, track 8 jumps to the neighboring cell that is supposed to be track 10 from frame 588, and is eventually switched with track 10 in frame 591.

We use the Kalman filter [33] with a random walk model for the cell motion:

$$\mathbf{s}_t = \mathbf{A}\mathbf{s}_{t-1} + \mathbf{w}_{t-1}, \quad (8)$$

$$\mathbf{y}_t = \mathbf{H}\mathbf{s}_t + \mathbf{v}_t. \quad (9)$$

The state vector \mathbf{s}_t includes the position and velocity of a cell in frame t , i.e., $\mathbf{s}_t = [x, y, \dot{x}, \dot{y}]^T$ and the measurement vector \mathbf{y}_t is the measurements of the states. \mathbf{w}_t and \mathbf{v}_t represent the process and measurement noises, which are independent zero-mean normal distribution with covariances \mathbf{Q} and \mathbf{R} , respectively. In this filter, we set \mathbf{A} and \mathbf{H} to be identity matrices and determine the error covariances \mathbf{Q} and \mathbf{R} from training sequences, which are defined as follows:

$$\mathbf{Q} = \begin{bmatrix} 0.1 & 0 & 0 & 0 \\ 0 & 0.1 & 0 & 0 \\ 0 & 0 & 0.01 & 0 \\ 0 & 0 & 0 & 0.01 \end{bmatrix}, \quad \mathbf{R} = \begin{bmatrix} 0.1 & 0 \\ 0 & 0.1 \end{bmatrix}. \quad (10)$$

Thus, the predicted position of a cell is set to be the position of the cell in the previous frame, and then is corrected by the position of the cell in the current frame.

When the filter is applied to the detected positions given in Fig. 10(a), the tracking result is shown in Fig. 10(b). In frame 589, the position of track 8 is adjusted between the two positions corresponding to track 8 in frame 588 and 589 of Fig. 10(a), which prevents a track switching and maintains track 8 correctly on the same cell although the cell is not detected in frames 589 and 590 as shown in Fig. 10(a).

III. CELL CULTURE AND IMAGING

Bone marrow CD34+ HSCs (Stem Cell Technologies, Vancouver, BC, Canada) were cultured in serum-free expansion media with Stem Span Cocktail CC100 (Stem Cell Technologies, Vancouver, BC, Canada) at 37°C, 5% CO₂. The cells were seeded in microwells at a density of 1-5 cells/well.

Time-lapse images were taken on 0.5-minute intervals for 4 days using a Carl Zeiss Axiovert 200M microscope with an EC-Plan Neofluar 5× phase objective (Carl Zeiss Microimaging, Thornwood, NY), a heated stage incubator at 37°C, 5% CO₂, and 90% humidity (Pathology Devices Inc., Westminster, MD), and AxioVision 4.7.1 software. The images have 1388 × 1040 pixels and include a 3 × 5 array of microwells. There are two reasons for using 5× magnification images. First, more wells in the field of view enables more experiments to be conducted, performed in parallel, allowing for higher experimental throughput. Second, the halo effect for the cells appears more prominent compared to size, which makes the cells more spherical in appearance.

IV. EXPERIMENTS

The experiments were carried out in Matlab on Dell Precision T7500 (Xeon E5504/12GB RAM). Processing time is about 1 second per frame for an input of 600×600 pixels which contains a single well as in Fig. 1. We tested four sequences, each of which consists of 11520 frames, and the tracking performance was evaluated on lineage trees constructed from a tracking result and ground truth. Ground truth was created semi-automatically. Since it is very inefficient to annotate all cells, we first detected all possible cell locations automatically and then corrected them manually. In order to facilitate this job, we developed a GUI-based correction program. Two people worked on the ground truthing by splitting the sequences into two sets. After finishing each set, they double checked the ground truth each other.

Fig. 11 shows the evaluation result for one of the sequences. We used two metrics for the evaluation which were introduced in the radar literature [28]: *track purity* and *target effectiveness*. Track purity is the measure of how pure the trajectories of tracking results are. In other words, a track that consistently follows the same cell over time has high purity, while a track that is associated with multiple cells together incorrectly has low purity. The metric is computed as

$$TP(i) = L(i, j)/L(i), \quad (11)$$

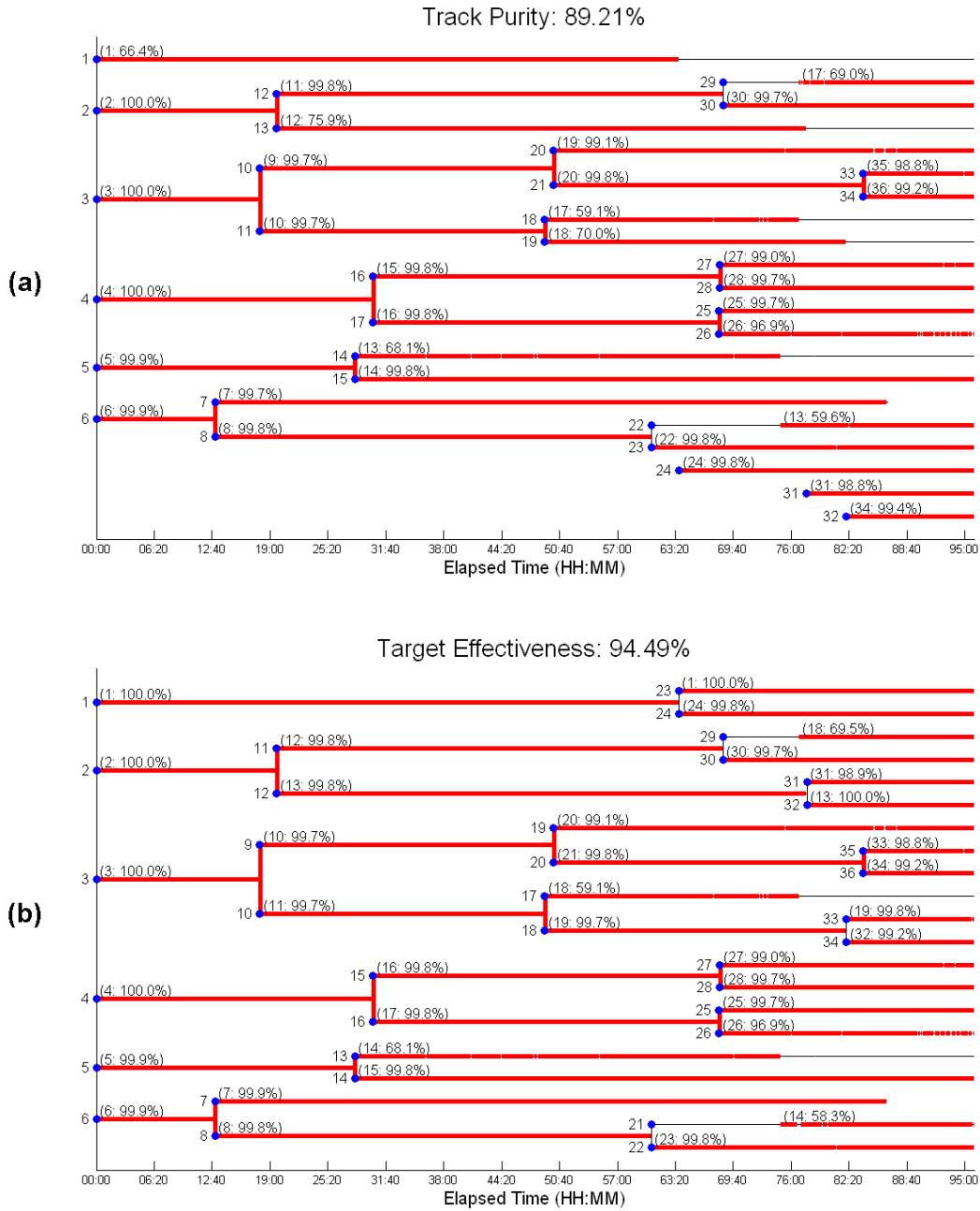


Fig. 11. Tracking performance evaluation with lineage trees in terms of (a) track purity and (b) target effectiveness. The red lines in (a) indicate correctly tracked parts in the whole trajectories of a tracking result which are denoted with a black line, while the red ones in (b) indicate correctly tracked parts in the ground truth. If tracking is perfect, red lines will cover all black lines. In (a)/(b), the numbers located in front of horizontal lines are track/cell IDs, and the two numbers in the brackets are cell/track IDs corresponding to the tracks/cells and their track purity/target effectiveness values, respectively.

where $L(i, j)$ is the length (number of frames) of track i assigned to cell j that is the most assigned among true cells with the track, and $L(i)$ is the total length of track i .

Track purity, however, does not penalize tracks that are deleted earlier or are formed later than actual cell trajectories. Thus the second metric, target effectiveness, is required. The target effectiveness is defined from the opposite viewpoint as follows:

$$TE(j) = L(j, i)/L(j), \quad (12)$$

where $L(j, i)$ is the length of trajectory of a true cell, target

j assigned to track i that is most assigned among tracks with the trajectory, and $L(j)$ is the total length of the trajectory of the true cell, target j .

For track purity, the lineage trees of a tracking result (thin black lines in Fig. 11(a)) are first drawn where horizontal lines correspond to individual tracks, and then ground truth (thick red lines in Fig. 11(a)) correctly associated with the tracks is overlaid on the lineage trees. When a track is divided into two tracks, new track IDs are assigned and if a mother-daughter relationship is correctly established, it is represented

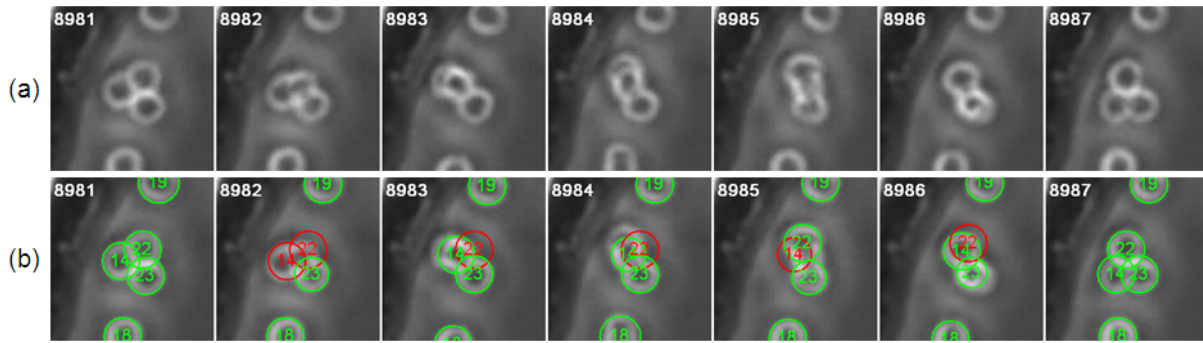


Fig. 12. Example of severe occlusion resulting in tracking error. (a) Input image sequence. (b) The resulting track swap between track 14 and 22; the numbers in circles represent track IDs, the green circles are continuously associated tracks, and the red ones are temporarily lost tracks.

TABLE I
DETECTION AND TRACKING ACCURACY (%)

Sequence	# of frames	# of cells	Detection		Tracking	
			Precision	Recall	TP	TE
1	11520	82189	98.6	96.5	92.2	98.1
2	11520	120990	98.3	97.2	85.0	91.3
3	11520	137521	96.6	96.0	86.6	87.1
4	11520	147023	98.5	98.2	89.2	94.5
Overall	46080	487723	98.0	97.0	88.3	92.8

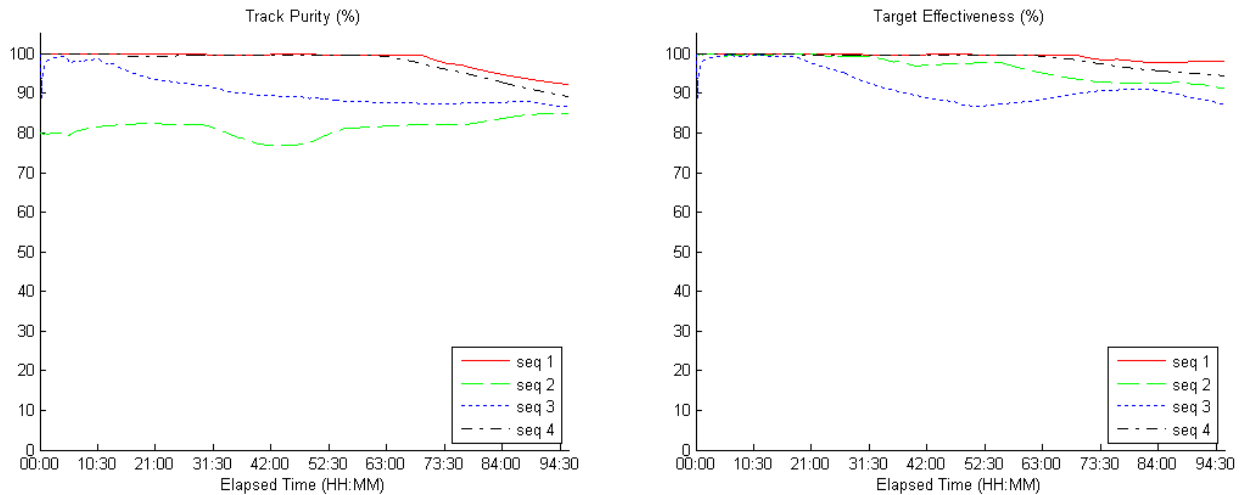


Fig. 13. Accumulated track purity (left panel) and target effectiveness (right panel) over time for the four test sequences. Given a specific time, the metrics are computed with only tracks that are formed until the time. It is shown that the overall performance has a tendency to reduce somewhat since the number of cells increases and they more often touch and overlap as shown in Fig. 12. The final values in the last frame correspond to the TP and TE shown in Table 1.

by a vertical thick red line between the two tracks. The overall track purity is the total length of correctly tracked segments divided by the total length of lineage trees.

As mentioned earlier, if a track is continuously associated with the same cell, the red line will be long and the track purity will be high. But the red lines can be partly broken when cells are lost and later successfully linked or come back. In our experiments, the detection accuracy was very high and so there were few broken lines. In the case of cell death (apoptosis), the red line is terminated early as track 7 in Fig. 11(a).

The target effectiveness of Fig. 11(b) is explained in exactly the same manner after replacing the roles of tracks and ground truth each other. The two metrics on lineage trees are useful to not only see the overall performance, but also examine how a

tracking system works and what problems occur. For example, we can see that track 14 failed to follow cell 13 around 75h and unfortunately moved to another cell (cell 21). Looking at the image sequence around that time (Fig. 12), a severe occlusion started to occur in frame 8982. That caused false negatives and eventually track switching; for the almost complete occlusion, it would be better to allow users to make a decision if it is critical in analyzing stem cell behaviors.

Table I summarizes the detection and tracking results for all the sequences. The detection accuracy was evaluated in terms of *precision* $TP/(TP+FP)$ and *recall* $TP/(TP+FN)$, where TP, FP, and FN denote the number of true positives, false positives, and false negatives, respectively. Our proposed method achieved 98.0% precision and 97.0% recall in detection, and

88.3% track purity and 92.8% target effectiveness in tracking. The first sequence showed the best tracking accuracy since the cell population is smaller than the others. As cells divide into daughter cells and the number of cells increases, they are more likely to touch and overlap one another, which reduces the overall performance. Fig. 13 shows the track purity and target effectiveness over time. Since the metrics were accumulated over time, they can increase for a certain period of time but finally reach the values shown in Table 1.

V. CONCLUSION

We proposed an automated tracking method for hematopoietic stem cells in phase contrast microscopy images. Our method exploits a data-association approach that assigns newly detected cells to tracks in each frame. The occurrence of mitotic events is identified in the spatio-temporal context during the association. The method was extensively validated in thousands of images, achieving 88.3% track purity and 92.8% target effectiveness. Based on the high accuracy measurements, the method will facilitate the study of HSCs under different culture conditions in an effort to optimize cell expansion for therapeutic purposes.

ACKNOWLEDGMENT

We would like to thank Drs. K. Li, Z. Yin, and M. Chen for their valuable suggestions and comments. This work was supported in part by the National Institutes of Health Grants R01 EB07369-01 and R01 EB04343-01.

REFERENCES

- [1] S. M. Watt, E. Austin, and S. Armitage, "Cryopreservation of hematopoietic stem/progenitor cells for therapeutic use," *Methods in Molecular Biology*, vol. 368, pp. 237–259, 2007.
- [2] C. Gekas, K. E. Rhodes, and H. K. A. Mikkola, "Isolation and analysis of hematopoietic stem cells from the placenta," *Journal of Visualized Experiments*, no. 16, 2008. [Online]. Available: <http://www.jove.com/index/details.stp?id=742>
- [3] S. S. Kelly, C. B. S. Sola, M. de Lima, and E. Shpall, "Ex vivo expansion of cord blood," *Bone Marrow Transplantation*, vol. 44, pp. 673–681, 2009.
- [4] T. Schroeder, "Hematopoietic stem cell heterogeneity: Subtypes, not unpredictable behavior," *Cell Stem Cell*, vol. 6, no. 3, pp. 203–207, 2010.
- [5] R. Möhle and L. Kanz, "Hematopoietic growth factors for hematopoietic stem cell mobilization and expansion," *Seminars in Hematology*, vol. 44, no. 3, pp. 193–202, 2007.
- [6] I. Martin, H. Baldomero, A. Tyndall, D. Niederwieser, and A. Gratwohl, "A survey on cellular and engineered tissue therapies in europe in 2008," *Tissue Engineering Part A*, 2010.
- [7] J. G. Sharp, A. Kessinger, J. C. Lynch, Z. S. Pavletic, and S. S. Joshi, "Blood stem cell transplantation: Factors influencing cellular immunological reconstitution," *Journal of Hematology and Stem Cell Research*, vol. 9, no. 6, pp. 971–981, 2000.
- [8] D. Padfield, J. Rittscher, N. Thomas, and B. Roysam, "Spatio-temporal cell cycle phase analysis using level sets and fast marching methods," *Medical Image Analysis*, vol. 13, no. 1, pp. 143–155, 2009.
- [9] K. Li, E. Miller, M. Chen, T. Kanade, L. Weiss, and P. Campbell, "Cell population tracking and lineage construction with spatiotemporal context," *Medical Image Analysis*, vol. 12, no. 5, pp. 546–566, 2008.
- [10] —, "Computer vision tracking of stemness," in *Proc. IEEE International Symposium on Biomedical Imaging*, 2008, pp. 847–850.
- [11] F. Yang, M. Mackey, F. Ianzini, G. Gallardo, and M. Sonka, "Cell segmentation, tracking, and mitosis detection using temporal context," in *Proc. International Conference on Medical Image Computing and Computer Assisted Intervention*, 2005, pp. 302–309.
- [12] A. Dufour, V. Shinin, S. Tajbakhsh, N. Guillen-Aghion, J. Olivo-Marin, and C. Zimmer, "Segmenting and tracking fluorescent cells in dynamic 3-d microscopy with coupled active surfaces," *IEEE Trans. Image Processing*, vol. 14, no. 9, pp. 1396–1410, 2005.
- [13] K. Althoff, J. Degerman, C. Wahlby, T. Thorlin, J. Fajerson, P. Eriksson, and T. Gustavsson, "Time-lapse microscopy and classification of in vitro cell migration using hidden markov modeling," in *Proc. IEEE International Conference Acoust Speech Signal Processing*, 2006, pp. 6023–6026.
- [14] O. Al-Kofahi, R. Radke, S. Goderie, Q. Shen, S. Temple, and B. Roysam, "Automated cell lineage construction: A rapid method to analyze clonal development established with murine neural progenitor cells," *Cell Cycle*, vol. 5, no. 3, pp. 327–335, 2006.
- [15] N. Kachouie, P. Fieguth, J. Ramunas, and E. Jervis, "Probabilistic model-based cell tracking," *International Journal of Biomedical Imaging*, 2006.
- [16] T. Kirubarajan, Y. Bar-Shalom, and K. Pattipati, "Multiassignment for tracking a large number of overlapping objects," *IEEE Trans. on Aerospace and Electronic Systems*, vol. 37, no. 1, pp. 2–21, 2001.
- [17] D. Padfield, J. Rittscher, and B. Roysam, "Coupled minimum-cost flow cell tracking," in *Proc. Information Processing in Medical Imaging*, 2009, pp. 374–385.
- [18] R. Bise, K. Li, S. Eom, and T. Kanade, "Reliably tracking partially overlapping neural stem cells in dic microscopy image sequence," in *Proc. MICCAI Workshop on Optical Tissue Image analysis in Microscopy, Histopathology and Endoscopy*, 2009, pp. 67–77.
- [19] T. Cormen, C. Leiserson, R. Rivest, and C. Stein, *Introduction to Algorithms*. The MIT Press, 2001.
- [20] T. J. Atherton and D. J. Kerbyson, "Size invariant circle detection," *Image and Vision Computing*, vol. 17, pp. 795–803, 1999.
- [21] M. Smereka and I. Duleba, "Circular object detection using a modified hough transform," *Int. J. Appl. Math. Comput. Sci.*, vol. 18, no. 1, pp. 85–91, 2008.
- [22] T. Peng, A. Balijepalli, S. K. Gupta, and T. LeBrun, "Algorithms for on-line monitoring of micro spheres in an optical tweezers-based assembly cell," *Transactions of the ASME*, vol. 7, pp. 330–338, 2007.
- [23] B. Kumar, A. Mahalanobis, and R. D. Juday, *Correlation Pattern Recognition*. Cambridge University Press, 2005.
- [24] L. Miroslaw, A. Chorazyczewski, F. Buchholz, and R. Kittler, "Correlation-based method for automatic mitotic cell detection in phase contrast microscopy," in *Proc. Int. Conf. Computer Recognition Systems*, 2005, pp. 627–634.
- [25] N. N. Kachouie, L. J. Lee, and P. Fieguth, "A probabilistic living cell segmentation model," in *Proc. IEEE ICIP*, 2005, pp. 901–904.
- [26] N. N. Kachouie, P. Fieguth, J. Ramunas, and E. Jervis, "Probabilistic model-based cell tracking," *Int. J. Biomed. Imag.*, vol. 2006, pp. 1–10, 2006.
- [27] S. Eom, R. Bise, and T. Kanade, "Detection of hematopoietic stem cells in microscopy images using a bank of ring filters," in *The IEEE International Symposium on Biomedical Imaging*, April 2010, pp. 137–140.
- [28] S. Blackman and R. Popoli, *Design and Analysis of Modern Tracking Systems*. Artech House Publishers, 1999.
- [29] S. Huh, D. Ker, R. Bise, M. Chen, and T. Kanade, "Automated mitosis detection of stem cell populations in phase-contrast microscopy images," *IEEE Trans. Med. Imag.*, vol. 30, no. 3, pp. 586–596, 2011.
- [30] B. Kumar, A. Mahalanobis, and R. D. Juday, *Correlation Pattern Recognition*. Cambridge University Press, 2005.
- [31] S. Blackman, *Multiple-target tracking with radar applications*. Artech House, Inc., 1986.
- [32] F. Bourgeois and J. Lassalle, "An extension of the munkres algorithm for the assignment problem to rectangular matrices," *Communications of the ACM*, vol. 14, no. 12, p. 802, 1971.
- [33] G. Welch and G. Bishop, "An introduction to the kalman filter," University of North Carolina at Chapel Hill, Tech. Rep., 2006.